Earthq Eng & Eng Vib (2019) 18: 35-52 **DOI**: https://doi.org/10.1007/s11803-019-0488-7

A modified domain reduction method for numerical simulation of wave propagation in localized regions

Luo Chao[1,2†], Lou Menglin[1‡], Gui Guoqing[3‡] and Wang Hao[1,2†]

1. *School of Civil Engineering, Shijiazhuang Tiedao University, Hebei 050043, China; Cooperative Innovation Center of Disaster Prevention and Mitigation for Large Infrastructure in Hebei province* (*Shijiazhuang Tiedao University*)
2. *State Key Laboratory of Disaster Reduction in Civil Engineering, Tongji University, Shanghai 200092, China*
3. *School of Architecture and Civil Engineering, Jinggangshan University, Jiangxi 343009, China*

Abstract: A modified domain reduction method (MDRM) that introduces damping terms to the original DRM is presented in this paper. To verify the proposed MDRM and compare the computational accuracy of these two methods, a numerical test is designed. The numerical results of the MDRM and DRM are compared using an extended meshed model. The results show that the MDRM significantly improved the computational accuracy of the DRM. Then, the MDRM is compared with two existing conventional methods, namely Liao's transmitting boundary and viscous-spring boundary with Liu's method. The MDRM shows its great advancement in computational accuracy, stability and range of applications. This paper also discusses the influence of boundary location on computational accuracy. It can be concluded that smaller models tend to have larger errors. By introducing two dimensionless parameters, φ_1 and φ_2, the rational distance between the observation point and the MDRM boundary is suggested. When $\varphi_1 > 2$ or $\varphi_2 > 13$, the relative PGA error can be limited to 5%. In practice, the appropriate model size can be chosen based on these two parameters to achieve desired computational accuracy.

Keywords: modified domain reduction method; domain reduction method; viscous boundary; viscous spring boundary; transmitting boundary; wave propagation

1 Introduction

When simulating earthquake ground motion of a site with significant topography by numerical methods such as the finite element method, a large computation domain is usually required to mimic the theoretically infinite soil domain. When using the finite element method as a simulation approach, the maximum grid size of a finite element model is proportional to the shear wave velocity of the material and inversely proportional to the highest relevant frequency of the excitation. This maximum grid size is usually small compared to the whole computation domain. Given that, a finite element model simulating seismic wave propagation will need to be meshed into numerous elements and nodes. Because of this, the analysis of a rational 3D soil-structure interaction finite element model is still an extremely time consuming process, although computational tools have been greatly improved in the last half century.

In the past few decades, researchers have made great efforts to reduce the computation domain. One way is to develop artificial boundaries, which prevent unnecessary reflection waves from the edge of the numerical model with a finite size.

One of artificial boundaries proposed by Lindman (Lindman, 1975) is the transmitting boundary, in which projection operators are portrayed as an infinite region. Liao *et al*. (Liao *et al*., 1984; Liao *et al*., 1984) proposed a simple and practical transmitting boundary that could be easily implemented into finite elements or finite differences. Liao's transmitting boundary is a higher order boundary and is convenient for finite element applications, but it may lead to dynamic instabilities for high frequencies (Kausel, 1988). The mechanism of drift instability and oscillation instability and their prevention measures aimed at Liao's transmitting boundary have been discussed by many researchers (Liao *et al*., 1992; Guan *et al*., 1996; Li *et al*., 1996; Zhou *et al*., 2001; Liao *et al*., 2002; Jing *et al*., 2002; Xie *et al*., 2017).

Another type of artificial boundary is the viscous boundary (Lysmer *et al*., 1969), which uses dashpots at the boundary instead of the far field. The viscous

Correspondence to: Luo Chao, School of Civil Engineering, Shijiazhuang Tiedao University, Hebei 050043, China
Tel: + 86-18733138268
E-mail: luochao@stdu.edu.cn
†Lecturer; ‡Professor

Supported by: National Natural Science Foundation of China under Grant Nos. 91315301, 51478279 and the State Key Laboratory Basic Theory Foundation of the Ministry of Science and Technology of China under the Grant SLDRCE08-A-07
Received March 27, 2017; **Accepted** November 3, 2017

boundary can be applied directly to solve the internal source problems, which means the real excitation is located in the computation domain. For external source problems like soil-structure interaction (SSI) problems and site response analysis, the real excitation is difficult to model because it is located outside the computation domain. In such circumstances, the excitation is usually performed as some equivalent forces, by which an external source problem can be converted into an "internal" source problem so that it can incorporate with the viscous boundary. Many researchers focus on modelling the real excitation with equivalent forces. Joyner *et al*. (Joyner *et al*., 1975; Lysmer, 1978) proposed a method for one-dimensional (1D) wave propagation analysis, in which a horizontal equivalent force time history was incorporated with dashpots at the base of the soil column to realize the external source excitation. The Joyner's method has been widely used (Liang *et al*., 2017, Huang *et al*., 2018) Yasui *et al*. (1988) introduced angle dependent viscous dashpots and seismic waves for inclined wave excitation. Liu *et al*. (1998) extended the range of realizing the equivalent excitation from 1D wave propagation to inclined wave and multiple support excitation, based on the assumption that the displacement wave field and the stress wave field should be equal to the original ones.

The domain reduction method (DRM) proposed by Bielak *et al*. (Bielak *et al*., 2003; Yoshimura *et al*., 2003) is a finite element methodology for modeling earthquake ground motion in highly heterogeneous localized regions with large contrasts in wavelengths. It is developed for external source problems and can model all realistic seismic waves including body waves (SV, SH, P) and surface waves (Rayleigh, Love, etc.) (Jeremić *et al*., 2015). The performance of the DRM was assessed in conjunction with two commonly used absorbing boundaries, namely, the cone boundary (Kellezi, 2000) and the standard viscous boundary, and the cone boundary was found to be slightly superior to the viscous boundary. (Kontoe *et al*., 2009). The DRM was also extended by Kontoe *et al*. to deal with the dynamic coupled consolidation problems (Kontoe *et al*., 2008). As an advanced simulation method, the DRM significantly reduced the computational cost and improved the computational efficiency, and has been widely used in recent years. Kontoe *et al*. studied the seismic response of the Bolu highway twin tunnels by using the DRM (Kontoe *et al*., 2008). Jeremić *et al*. (2009) simulated the seismic SSI response for bridge structures on non-uniform soils. Corigliano *et al*. (2011) discussed the near fault effect of deep tunnels under seismic excitation. Kontoe *et al*. (2012) examined the seismic response of a large and complex system comprising a lock chamber and three neighboring waver saving basins. Jeremić *et al*. (2013) investigated the seismic response of a massive NPP structure due to full 3D, inclined, uncorrelated input motions for different and rock profiles. Isbiliroglu *et al*. (2015) analyzed the soil-structure interaction and coupling effects of various arrangements of regular building clusters during earthquakes. Solberg *et al*. (2016) derived a modified version of the DRM for nonlinear time-domain analysis and applied it to the seismic response analysis of a notional small modular reactor. Poursartip *et al*. (2017) deployed a simulating tool which integrated the perfectly-matched-layers, the unstructured spectral elements and the DRM and applied in a parametric study of seismic wave amplification by topographic features.

Through the references listed above, the advantages of the DRM in simulating complex wave propagation problems are clear; however, it has some shortcomings. First and foremost, to decrease the storage cost of computation, this method does not introduce damping terms in the computation of equivalent excitation forces. The influence of ignoring damping terms in the derivation has not yet been studied. Moreover, there is no basis or discussion for the selection of the DRM boundary location. In previous research related to the DRM, numerical models with a considerable material damping ratio which exceeds 10% are frequent, especially when the soil medium is included in the model (Kontoe *et al*., 2008; Kontoe *et al*., 2012; Isbiliroglu *et al*., 2015; Solberg *et al*., 2016). In such circumstances, the potential error caused by ignoring the damping terms could be large. However in the literature, the DRM that neglects the damping terms is used. The potential error caused by ignoring the damping terms in the DRM has never been discussed. Similarly, the DRM boundary is placed arbitrarily in all the applications, which may also reduce the accuracy of the results.

In this study, a modified domain reduction method (MDRM) is proposed, which considers damping terms on the basis of the DRM. A numerical example is given to study the effect of ignoring damping terms on the computational accuracy for different material damping ratios. The results using the MDRM and the DRM are compared. Then the computational accuracy of the MDRM is compared with the other two conventional methods; the transmitting boundary and the viscous-spring boundary. Finally, the influence of the MDRM boundary location on the computational accuracy is discussed. Furthermore, suggestions for selecting the boundary location are made by showing several examples.

2 Formulation of modified domain reduction method

A semi-infinite region that takes the earthquake source, propagation path, and local site features into consideration is shown in Fig.1 (a), where $P_e(t)$ denotes the earthquake source. Generally speaking, the location of the earthquake source is far away from the local site, relative to the size of the local site itself. In order to focus on the local site region of interest, a fictitious

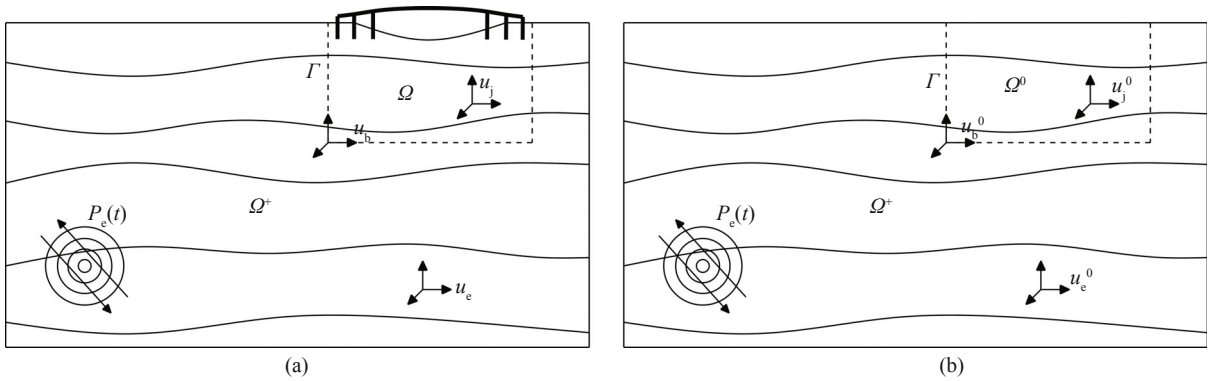

Fig. 1 (a) large physical domain with the source of load and local feature (b) Simplified large physical domain

boundary Γ is used to divide the semi-infinite region into two parts: Ω and Ω^+. Ω contains the local features of interest, like topography, foundations and structures located above, and Ω^+ is assumed as the remaining semi-infinite exterior subdomain. The displacement field for the exterior domain Ω^+, boundary Γ and interior domain Ω are denoted as u_e, u_b and u_i, respectively. Then, the equations of motion for the entire semi-infinite domain system can be written in the finite element expression as:

$$\begin{bmatrix} M_{ii}^{\Omega} & M_{ib}^{\Omega} & 0 \\ M_{bi}^{\Omega} & M_{bb}^{\Omega}+M_{bb}^{\Omega+} & M_{be}^{\Omega+} \\ 0 & M_{eb}^{\Omega+} & M_{ee}^{\Omega+} \end{bmatrix} \begin{Bmatrix} \ddot{u}_i \\ \ddot{u}_b \\ \ddot{u}_e \end{Bmatrix} + \begin{bmatrix} C_{ii}^{\Omega} & C_{ib}^{\Omega} & 0 \\ C_{bi}^{\Omega} & C_{bb}^{\Omega}+C_{bb}^{\Omega+} & C_{be}^{\Omega+} \\ 0 & C_{eb}^{\Omega+} & C_{ee}^{\Omega+} \end{bmatrix} \begin{Bmatrix} \dot{u}_i \\ \dot{u}_b \\ \dot{u}_e \end{Bmatrix} + \begin{bmatrix} K_{ii}^{\Omega} & K_{ib}^{\Omega} & 0 \\ K_{bi}^{\Omega} & K_{bb}^{\Omega}+K_{bb}^{\Omega+} & K_{be}^{\Omega+} \\ 0 & K_{eb}^{\Omega+} & K_{ee}^{\Omega+} \end{bmatrix} \begin{Bmatrix} u_i \\ u_b \\ u_e \end{Bmatrix} = \begin{Bmatrix} 0 \\ 0 \\ P_e \end{Bmatrix} \tag{1}$$

where $\boldsymbol{K}$, $\boldsymbol{C}$ and $\boldsymbol{M}$ denote mass, damping and stiffness matrices respectively; i, e, and b refers to nodes in either the interior or exterior domain or on their common boundary; the superscripts Ω and Ω^+ refer to the domains over which the various matrices are defined.

Equation (1) can be written into the following two formulas:

$$\begin{bmatrix} M_{ii}^{\Omega} & M_{ib}^{\Omega} \\ M_{bi}^{\Omega} & M_{bb}^{\Omega} \end{bmatrix} \begin{Bmatrix} \ddot{u}_i \\ \ddot{u}_b \end{Bmatrix} + \begin{bmatrix} C_{ii}^{\Omega} & C_{ib}^{\Omega} \\ C_{bi}^{\Omega} & C_{bb}^{\Omega} \end{bmatrix} \begin{Bmatrix} \dot{u}_i \\ \dot{u}_b \end{Bmatrix} + \begin{bmatrix} K_{ii}^{\Omega} & K_{ib}^{\Omega} \\ K_{bi}^{\Omega} & K_{bb}^{\Omega} \end{bmatrix} \begin{Bmatrix} u_i \\ u_b \end{Bmatrix} = \begin{Bmatrix} 0 \\ P_b \end{Bmatrix} \tag{2}$$

$$\begin{bmatrix} M_{bb}^{\Omega+} & M_{be}^{\Omega+} \\ M_{eb}^{\Omega+} & M_{ee}^{\Omega+} \end{bmatrix} \begin{Bmatrix} \ddot{u}_b \\ \ddot{u}_e \end{Bmatrix} + \begin{bmatrix} C_{bb}^{\Omega+} & C_{be}^{\Omega+} \\ C_{eb}^{\Omega+} & C_{ee}^{\Omega+} \end{bmatrix} \begin{Bmatrix} \dot{u}_b \\ \dot{u}_e \end{Bmatrix} + \begin{bmatrix} K_{bb}^{\Omega+} & K_{be}^{\Omega+} \\ K_{eb}^{\Omega+} & K_{ee}^{\Omega+} \end{bmatrix} \begin{Bmatrix} u_b \\ u_e \end{Bmatrix} = \begin{Bmatrix} -P_b \\ P_e \end{Bmatrix} \tag{3}$$

P_b are the interaction forces on the local boundary. To simplify the problem, a free-field model is considered as shown in Fig. 1 (b), where all the local features in the interior domain are removed and the exterior domain remains unchanged. In this free-field model, the displacement field for the exterior domain, boundary and interior domain are denoted as u_e^0, u_b^0 and u_i^0, respectively. Then, Eq. (3) can be written as:

$$\begin{bmatrix} M_{bb}^{\Omega+} & M_{be}^{\Omega+} \\ M_{eb}^{\Omega+} & M_{ee}^{\Omega+} \end{bmatrix} \begin{Bmatrix} \ddot{u}_b^0 \\ \ddot{u}_e^0 \end{Bmatrix} + \begin{bmatrix} C_{bb}^{\Omega+} & C_{be}^{\Omega+} \\ C_{eb}^{\Omega+} & C_{ee}^{\Omega+} \end{bmatrix} \begin{Bmatrix} \dot{u}_b^0 \\ \dot{u}_e^0 \end{Bmatrix} + \begin{bmatrix} K_{bb}^{\Omega+} & K_{be}^{\Omega+} \\ K_{eb}^{\Omega+} & K_{ee}^{\Omega+} \end{bmatrix} \begin{Bmatrix} u_b^0 \\ u_e^0 \end{Bmatrix} = \begin{Bmatrix} -P_b^0 \\ P_e \end{Bmatrix} \tag{4}$$

The second equation in Eq. (4) can be written as follows:

$$P_e = M_{eb}^{\Omega+}\ddot{u}_b^0 + M_{ee}^{\Omega+}\ddot{u}_e^0 + C_{eb}^{\Omega+}\dot{u}_b^0 + C_{ee}^{\Omega+}\dot{u}_e^0 + K_{eb}^{\Omega+}u_b^0 + K_{ee}^{\Omega+}u_e^0 \tag{5}$$

Then a transformation of variables is introduced to simplify the analysis. The total displacement u_e can be expressed as the sum of the free field u_e^0 and the residual field ω_e as follows:

$$u_e = u_e^0 + \omega_e \tag{6}$$

By substituting Eq. (6) into Eq. (1) and moving all the terms that contain the free field to the right side results in:

$$\begin{bmatrix} M_{ii}^{\Omega} & M_{ib}^{\Omega} & 0 \\ M_{bi}^{\Omega} & M_{bb}^{\Omega}+M_{bb}^{\Omega+} & M_{be}^{\Omega+} \\ 0 & M_{eb}^{\Omega+} & M_{ee}^{\Omega+} \end{bmatrix} \begin{Bmatrix} \ddot{u}_i \\ \ddot{u}_b \\ \ddot{\omega}_e \end{Bmatrix} + \begin{bmatrix} C_{ii}^{\Omega} & C_{ib}^{\Omega} & 0 \\ C_{bi}^{\Omega} & C_{bb}^{\Omega}+C_{bb}^{\Omega+} & C_{be}^{\Omega+} \\ 0 & C_{eb}^{\Omega+} & C_{ee}^{\Omega+} \end{bmatrix} \begin{Bmatrix} \dot{u}_i \\ \dot{u}_b \\ \dot{\omega}_e \end{Bmatrix} + \begin{bmatrix} K_{ii}^{\Omega} & K_{ib}^{\Omega} & 0 \\ K_{bi}^{\Omega} & K_{bb}^{\Omega}+K_{bb}^{\Omega+} & K_{be}^{\Omega+} \\ 0 & K_{eb}^{\Omega+} & K_{ee}^{\Omega+} \end{bmatrix} \begin{Bmatrix} u_i \\ u_b \\ \omega_e \end{Bmatrix} = \begin{Bmatrix} 0 \\ -M_{be}^{\Omega+}\ddot{u}_e^0 - C_{be}^{\Omega+}\dot{u}_e^0 - K_{be}^{\Omega+}u_e^0 \\ -M_{ee}^{\Omega+}\ddot{u}_e^0 - C_{ee}^{\Omega+}\dot{u}_e^0 - K_{ee}^{\Omega+}u_e^0 + P_e \end{Bmatrix} \tag{7}$$

Substituting Eq. (5) into Eq. (7) results in:

$$\begin{bmatrix} M_{ii}^{\Omega} & M_{ib}^{\Omega} & 0 \\ M_{bi}^{\Omega} & M_{bb}^{\Omega}+M_{bb}^{\Omega+} & M_{be}^{\Omega+} \\ 0 & M_{eb}^{\Omega+} & M_{ee}^{\Omega+} \end{bmatrix} \begin{Bmatrix} \ddot{u}_i \\ \ddot{u}_b \\ \ddot{\omega}_e \end{Bmatrix} + \begin{bmatrix} C_{ii}^{\Omega} & C_{ib}^{\Omega} & 0 \\ C_{bi}^{\Omega} & C_{bb}^{\Omega}+C_{bb}^{\Omega+} & C_{be}^{\Omega+} \\ 0 & C_{eb}^{\Omega+} & C_{ee}^{\Omega+} \end{bmatrix} \begin{Bmatrix} \dot{u}_i \\ \dot{u}_b \\ \dot{\omega}_e \end{Bmatrix}$$
$$+ \begin{bmatrix} K_{ii}^{\Omega} & K_{ib}^{\Omega} & 0 \\ K_{bi}^{\Omega} & K_{bb}^{\Omega}+K_{bb}^{\Omega+} & K_{be}^{\Omega+} \\ 0 & K_{eb}^{\Omega+} & K_{ee}^{\Omega+} \end{bmatrix} \begin{Bmatrix} u_i \\ u_b \\ \omega_e \end{Bmatrix} = \begin{Bmatrix} 0 \\ -M_{be}^{\Omega+}\ddot{u}_e^0 - C_{be}^{\Omega+}\dot{u}_e^0 - K_{be}^{\Omega+}u_e^0 \\ M_{eb}^{\Omega+}\ddot{u}_b^0 + C_{eb}^{\Omega+}\dot{u}_b^0 + K_{eb}^{\Omega+}u_b^0 \end{Bmatrix} \tag{8}$$

In Eq. (8) the mass matrix, damping matrix and stiffness matrix on the left side are identical to those of Eq. (1). Thus, the seismic force P_e in equation can be replaced by the effective nodal forces P^{eff}, given by:

$$P^{\text{eff}} = \begin{Bmatrix} 0 \\ -M_{be}^{\Omega+}\ddot{u}_e^0 - C_{be}^{\Omega+}\dot{u}_e^0 - K_{be}^{\Omega+}u_e^0 \\ M_{eb}^{\Omega+}\ddot{u}_b^0 + C_{eb}^{\Omega+}\dot{u}_b^0 + K_{eb}^{\Omega+}u_b^0 \end{Bmatrix} \tag{9}$$

In Eq. (9), the damping matrix is required to compute the effective nodal forces P^{eff}. There is no specific requirement for using the damping model in the MDRM. Any damping model that is able to formulate the damping matrix can be used in the MDRM. If Eq. (8) is solved in the frequency domain, hysteretic damping can also be used to calculate the effective nodal forces P^{eff}.

In Bielak *et al*. (2003), the effective nodal forces P_0^{eff} were expressed as follows:

$$\boldsymbol{P}_0^{\text{eff}} = \begin{Bmatrix} 0 \\ -M_{be}^{\Omega+}\ddot{u}_e^0 - K_{be}^{\Omega+}u_e^0 \\ M_{eb}^{\Omega+}\ddot{u}_b^0 + K_{eb}^{\Omega+}u_b^0 \end{Bmatrix} \tag{10}$$

It can be seen that P^{eff} contains damping terms but P_0^{eff} does not. The modification of P^{eff} is how the MDRM improves on the DRM.

As in the DRM, the MDRM is a two-step method. In step I, a background geological model including the original earthquake source is analyzed to obtain the displacement fields u_b^0 and u_e^0, as shown in Fig. 1(b). Then P^{eff} is calculated by substituting u_b^0 and u_e^0 into Eq. (9). Any appropriate numerical and analytical approach that calculates the free-field wave fields can be incorporated in this step. In step II, the effective seismic forces P^{eff} act as the excitation on domain Ω. By solving Eq. (8), the total wave fields u_i and u_b, and the residual wave field ω_e are available. Because of the existing residual wave field ω_e, the MDRM has to be used with suitable absorbing boundary conditions, as in the DRM (Bielak *et al*., 2003). Kontoe *et al*. (2009) assessed the performance of two commonly used absorbing boundaries in conjunction with the DRM and showed that the cone boundary was slightly superior to the standard viscous boundary. In practice, any local transmitting boundaries (Kausel, 1988), such as viscous boundary (Lysmer *et al*., 1969), viscous-spring boundary (Liu *et al*. 1998), transmitting bounudary (Liao *et al*., 1984) and PML boundary (Berenger, 1994; Farzanian *et al*., 2016; Poursartip *et al*., 2017) etc., can be used in cooperation with the MDRM.

3 Numerical examples

In this section, to explore the potential error caused by ignoring the damping terms in the DRM, the performance of the proposed MDRM and the original DRM are assessed and compared with different damping ratios and input motions. To start with, establishing an appropriate verification model is very important. In the original DRM (Yoshimura *et al*., 2003), a two-layer elastic half-space model was used, where the excitation was a dip-slip double couple. In step I of this verification example, the free-field displacements were calculated by the Green's function method. Since the verification model did not consider the material damping, the lack of damping terms in P_0^{eff} had no influence on the results. This verification model is not appropriate for the MDRM as the damping of material is introduced. In step I of the MDRM, the damping employed by Green's function method is frequency-independent. However, in step II, the damping is computed in the time domain where a frequency-independent damping model is not available. As a result, the damping model is different in these two steps and the interference caused by this difference should be excluded when comparing the computational accuracy of the two methods. One way to eliminate the interference is to repeat Yoshimura's model in the time domain in step I, but this approach needs a huge computation domain which is extremely time consuming. An alternative way is to perform an SV wave propagation analysis so that the free-field motion in step I can be obtained through a 1D SV wave propagation analysis and the consistency between the damping model in step I and II can be guaranteed. Given the above, the computation accuracy of DRM and MDRM in this section are discussed through an SV wave propagation problem.

For an SV wave propagation problem, the free-field displacements can be achieved by performing a 1D finite element (FE) analysis in step I of the MDRM and the DRM. Here the input method proposed by Joyner *et al*. (Joyner *et al*., 1975) is selected instead of the widely used closed-form solution (Idriss *et al*., 1968) in the frequency domain to simulate an elastic half-space. Thus, both step I and step II can be computed in the time domain and the consistency in the damping model between step I and step II can be guaranteed. The damping model used in both step I and step II is Rayleigh damping. In all the models in this study, the two frequencies used for Rayleigh damping are 0.5 Hz and 0.35 Hz. A 1D soil

column model with a depth of 250m is considered in this section. Selected input motions are a Ricker wavelet (Mavroeidis *et al*., 2003) and an artificial bedrock wave of Shanghai. The prevailing frequency of the Ricker displacement is 4 Hz. The time history and FFT plots of accelerations are shown in Fig. 2 and Fig. 3, and the time history and FFT plots of displacements are shown in Fig. 4 and Fig. 5.

For step II, a 2D finite element model with an idealized valley is built, as shown in Fig. 6. This model has a width of 400 m and a depth of 240 m. In Fig. 6, the blue part is the computation domain of interest and the red part is the DRM (MDRM) layer which is used to calculate the effective forces P^{eff} (P_0^{eff}) in Eq. (9) (Eq. (10)). The magenta layer is the exterior layer which connects with the viscous-spring elements to dissipate the residual wave. The material property of the soil is shown in Table 1. A rational mesh size of the finite element model directly determines the accuracy of numerical simulation of wave propagation. In this study, 16 nodes per wavelength are required for a given frequency. Assuming that the highest frequency of interest is 10 Hz, the mesh size Δh can be calculated as follows:

$$\Delta h = \frac{\lambda_{\max}}{16} = \frac{500/10}{16} = 3.125 \tag{11}$$

In this study, a conservative mesh size of 2.5 m is used.

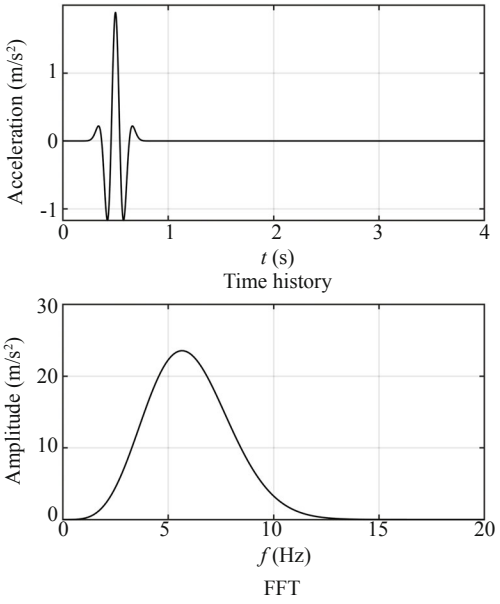

Fig. 2 Acceleration time history and FFT of Ricker wavelet

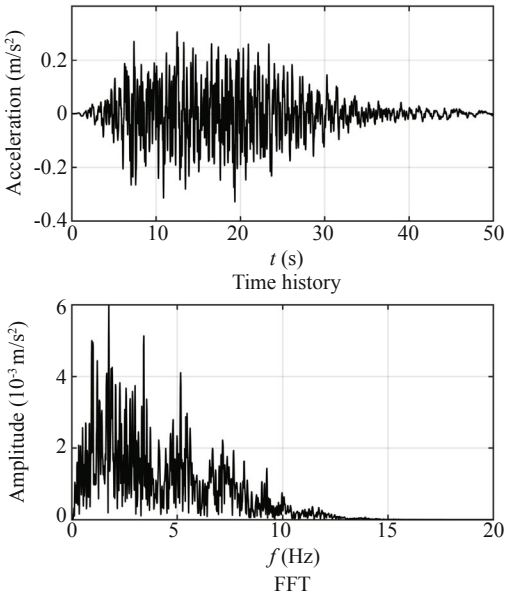

Fig. 3 Acceleration time history and FFT of bedrock motion

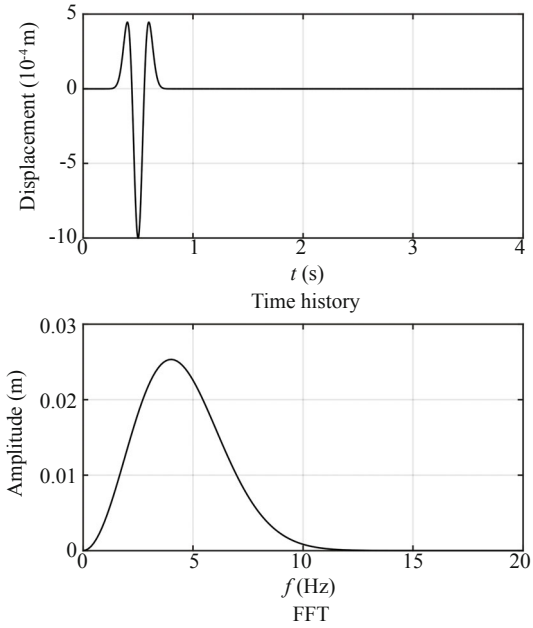

Fig. 4 Displacement time history and FFT of Ricker wavelet

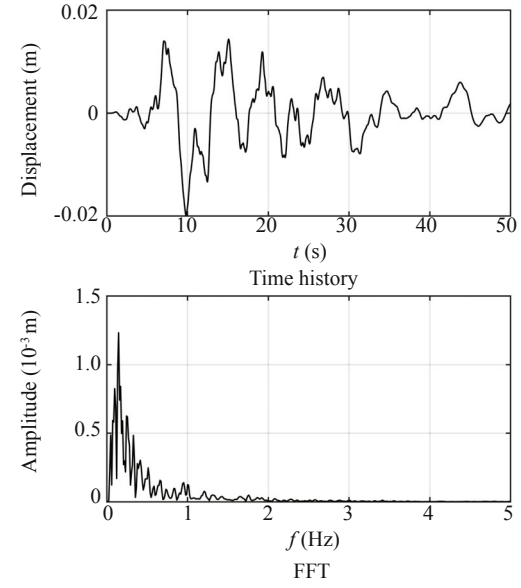

Fig. 5 Displacement time history and FFT of bedrock motion

Table 1 Material property

	Shear wave velocity (m/s)	Density (kg/m^3)	Poisson's ratio	Damping ratio (%)
Soil	500	2000	0.3	5

In this study, the Newmark-β method (Newmark, 1959) is used for time integration in all the analysis. The integration parameters of the Newmark-β method are set as $\gamma = 0.5$ and $\beta = 0.25$. No numerical damping is introduced in the time integration (Hilber *et al*., 1977).

In step I, the displacement, velocity and acceleration time histories of various depth are calculated through a 1D FE soil column model. The results will be used to calculate the equivalent forces P^{eff} and P_0^{eff} for the DRM and the MDRM. As mentioned above, local absorbing boundaries are placed on the 2D model. Based on previous research (Kontoe *et al*., 2009), the cone boundary, namely the viscous-spring boundary, has a good performance when used in conjunction with the DRM. In this study, the viscous-spring boundary is used with both the DRM and the MDRM. To verify and compare the performance of the DRM and the MDRM, an extended meshed 2D FE model with a width of 5000 m and a depth of 250 m is built. The input method (Joyner *et al*., 1975) used in the 1D model is also used here. Since the topography produces vertical motions, additional vertical dashpots are also placed at the bottom of the model. The results of the extended meshed model are treated as the accurate results to calculate the computational errors of the DRM and the MDRM.

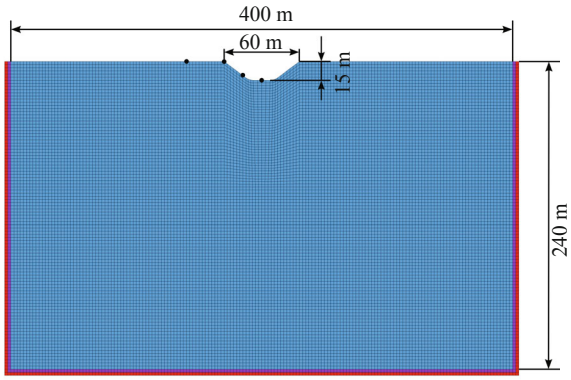

Fig. 6 Finite element mesh

In this section, the results of the DRM and the MDRM are compared through the 2D extended meshed model with different input motions and damping ratios. Damping ratios are set as 5% and 10%, respectively. The observation points can be found in Fig. 6. The analysis cases are shown in Table 2.

Figures 7 and 8 plot the horizontal and vertical acceleration response at each observation point in case 1. Figures 9 and 10 plot the horizontal and vertical

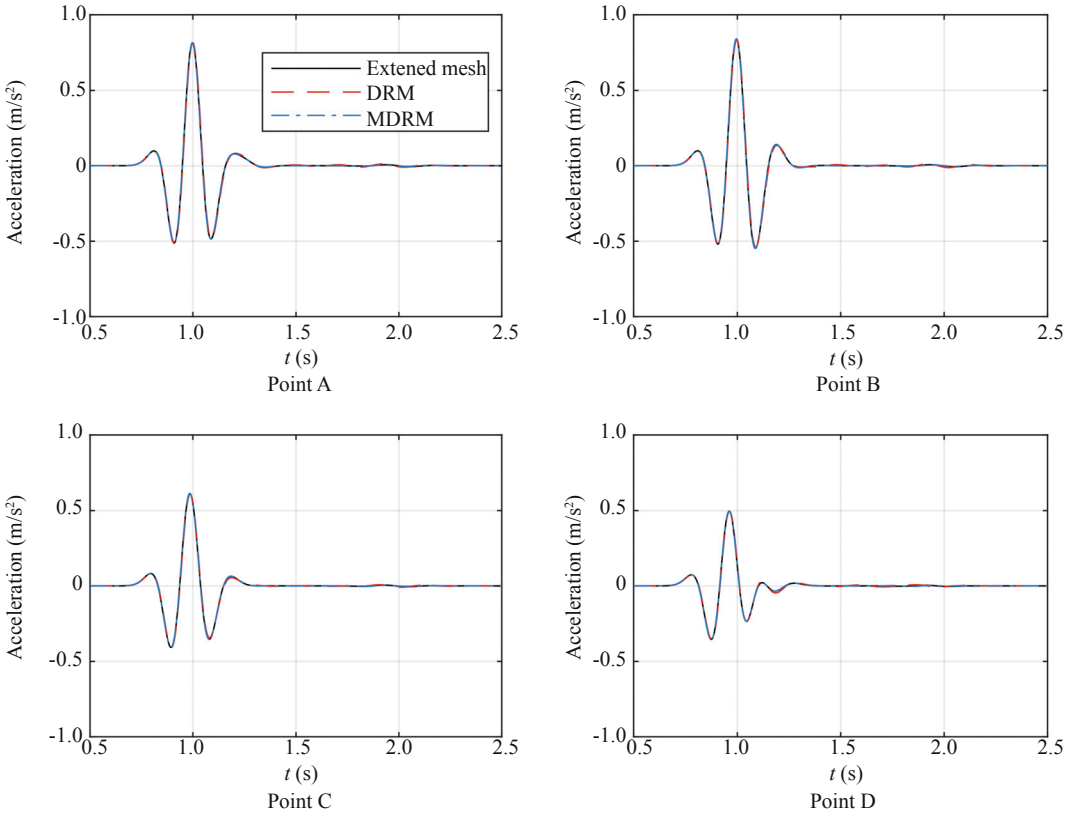

Fig. 7 Comparison of horizontal acceleration time history in case 1

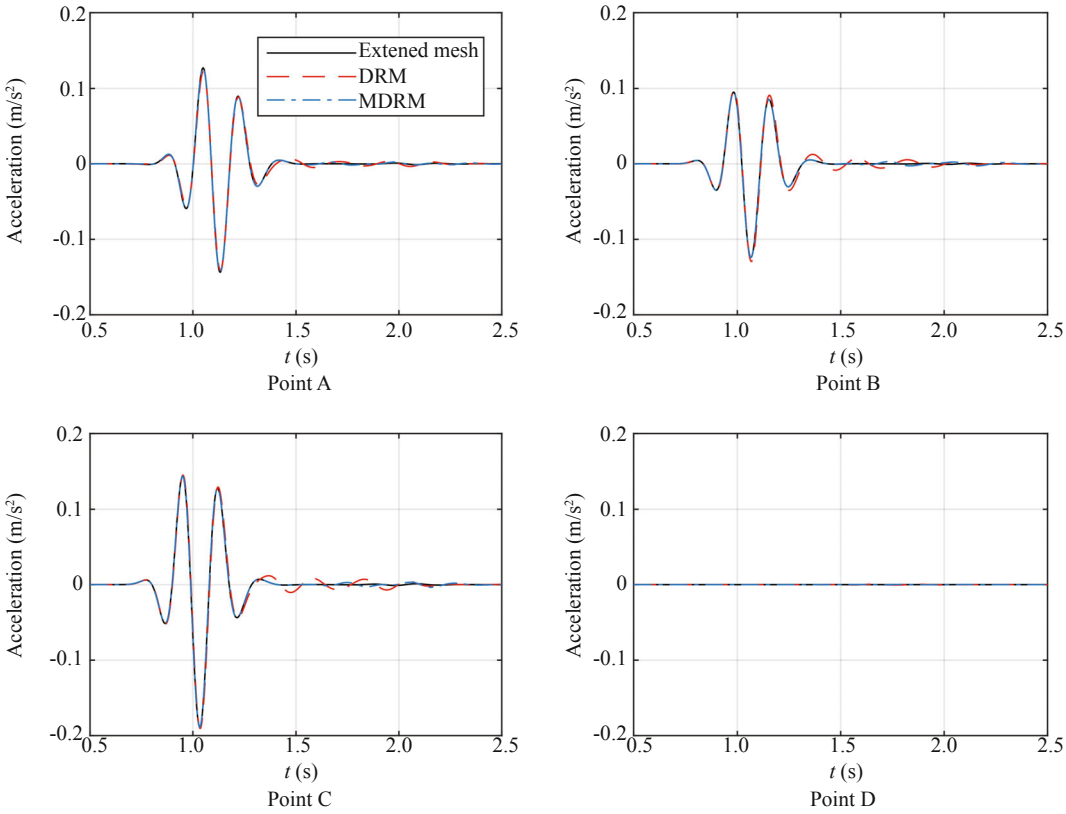

Fig. 8 Comparison of vertical acceleration time history in case 1

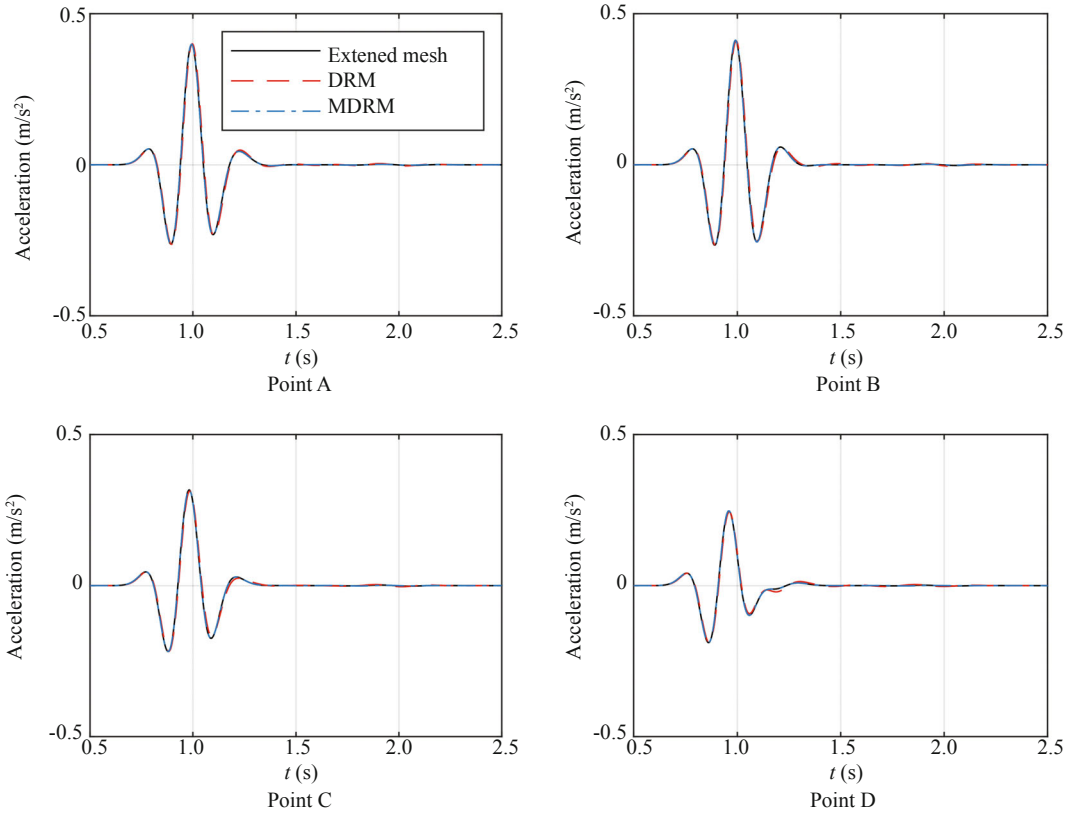

Fig. 9 Comparison of horizontal acceleration time history in case 2

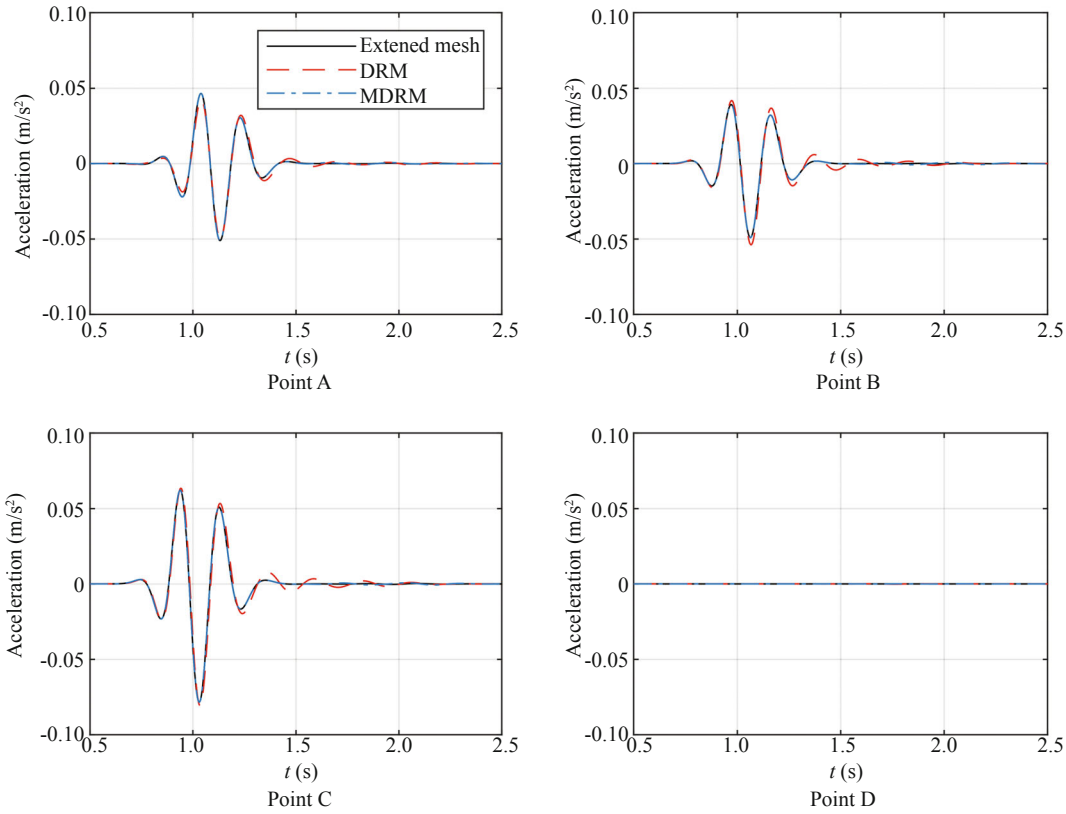

Fig. 10 Comparison of vertical acceleration time history in case 2

Table 2 Analyze cases

Analyze case	Damping ratio (%)	Input motion
Case 1	5%	Ricker wave
Case 2	10%	Ricker wave
Case 3	5%	Bedrock wave
Case 4	10%	Bedrock wave

acceleration response at each point in case 2. For case 3 and case 4, since the response has many high frequency components, plotting three time histories in a single figure makes the graph unclear. Thus, for case 3 and case 4, the extended mesh results and the absolute errors of the DRM and the MDRM are presented from Fig.11 to Fig.14. The PGA (peak ground acceleration) errors are listed from Table 3 to Table 6. As the observation point D, located on the axis of symmetry of topography, does not generate vertical response, the errors of its vertical PGA are not listed.

From case 1 to case 4, the horizontal and vertical responses at all the observation points are calculated. In all four cases, the accuracy of the horizontal response predicted by both the DRM and the MDRM is high. The maximum error of the horizontal acceleration associated with DRM and MDRM are 2.093% and 0.060%, respectively. However, the DRM loses accuracy in the vertical direction. For example, the maximum error of the vertical acceleration in case 4 of the DRM is as high as 32.441%. The relatively high error of the vertical response predicted by the DRM was also showed by Kontoe *et al*. (Kontoe *et al*., 2009). In the meantime, the MDRM still remains highly accurate in the vertical response; the maximum error in the vertical direction is as low as 2.136%.

The performance of the DRM and the MDRM using material with different damping ratios is also presented in these four cases. With the increase of the damping ratio, the accuracy of the DRM decreases. This phenomena can be easily explained by Eq. (9) and Eq. (10). The higher the material damping ratio, the larger the error of P_0^{eff} in Eq. (10), which results in the larger error of the response. As can be seen in case 4, the maximum error of the vertical acceleration produced by DRM is 32.441%, which is unacceptable in most circumstances.

By comparing Table 3 with Table 5 and Table 4 with Table 6, it can be seen that the DRM has a larger error when the input motion is bedrock motion, whereas the MDRM remains accurate. In case 1 and case 2, for the extended mesh model and the MDRM, the system becomes silent after 1.5 s, whereas at that time, the DRM still has residual waves in the system. For simple waves with a small quantity of zero crossing times, these residual waves have no influence on the upcoming peaks and valleys of the wave because the appearance time between peaks is long. However, when the input motion

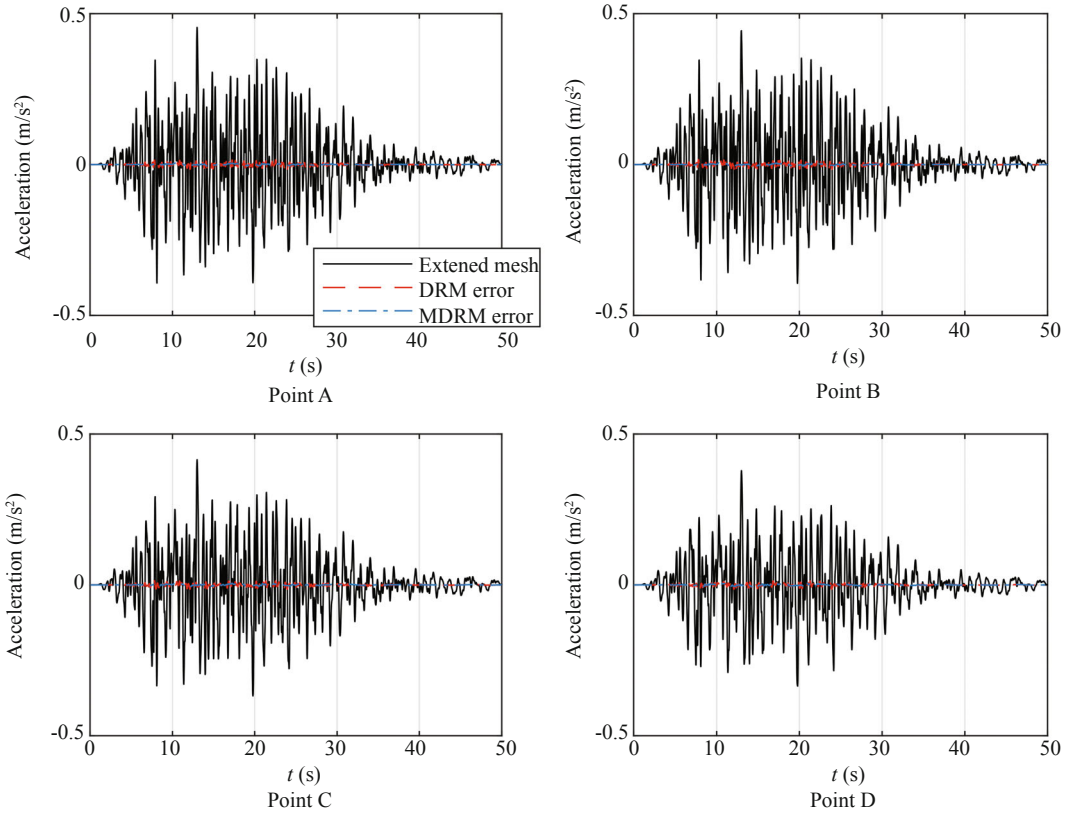

Fig. 11 Comparison of horizontal acceleration time history in case 3

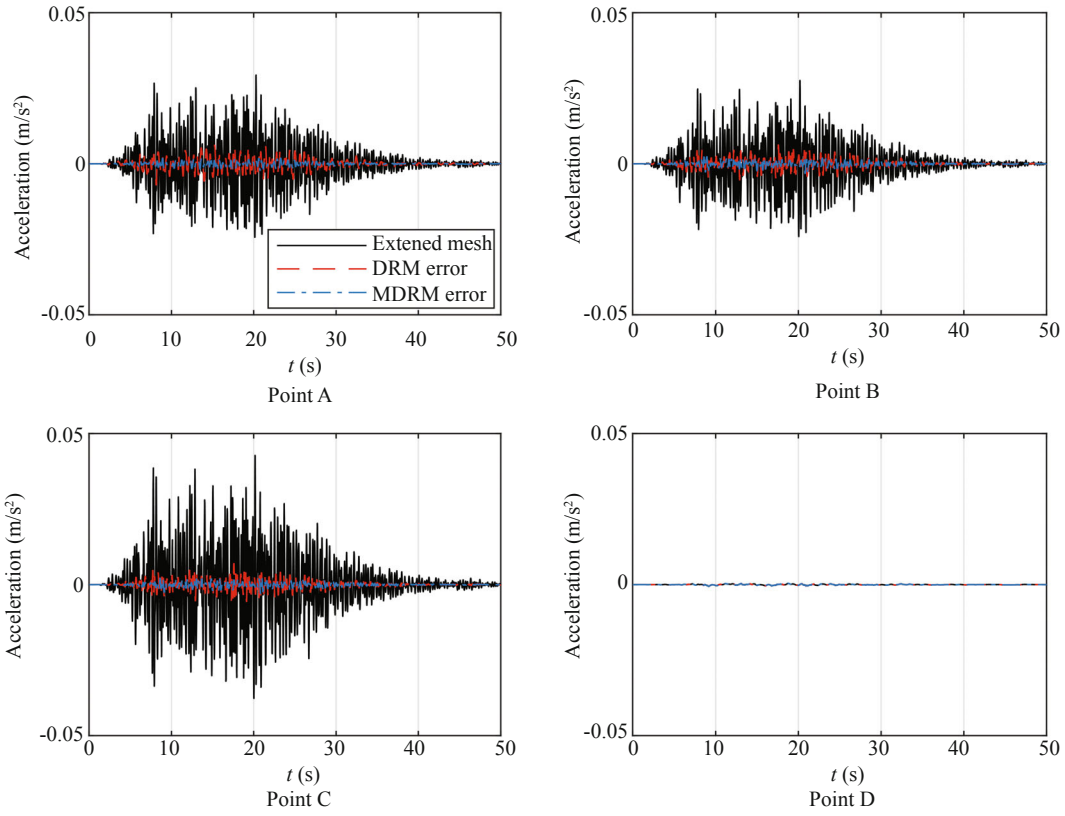

Fig. 12 Comparison of vertical acceleration time history in case 3

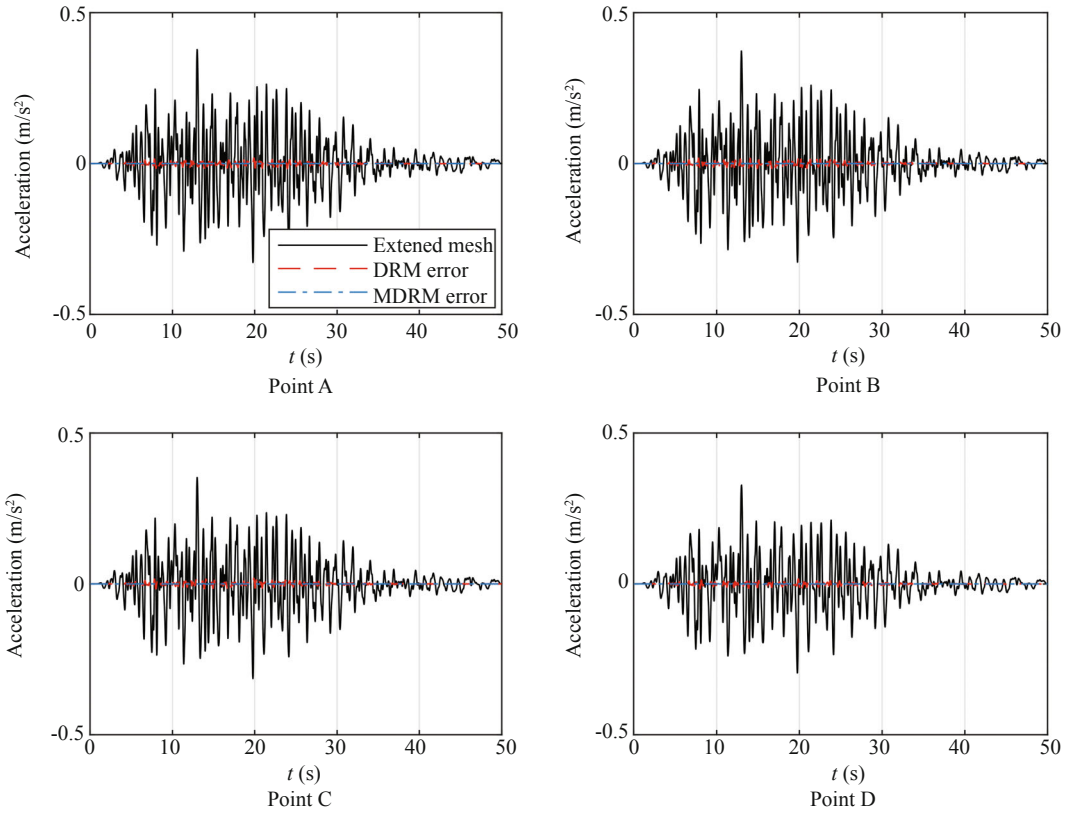

Fig. 13 Comparison of horizontal acceleration time history in case 4

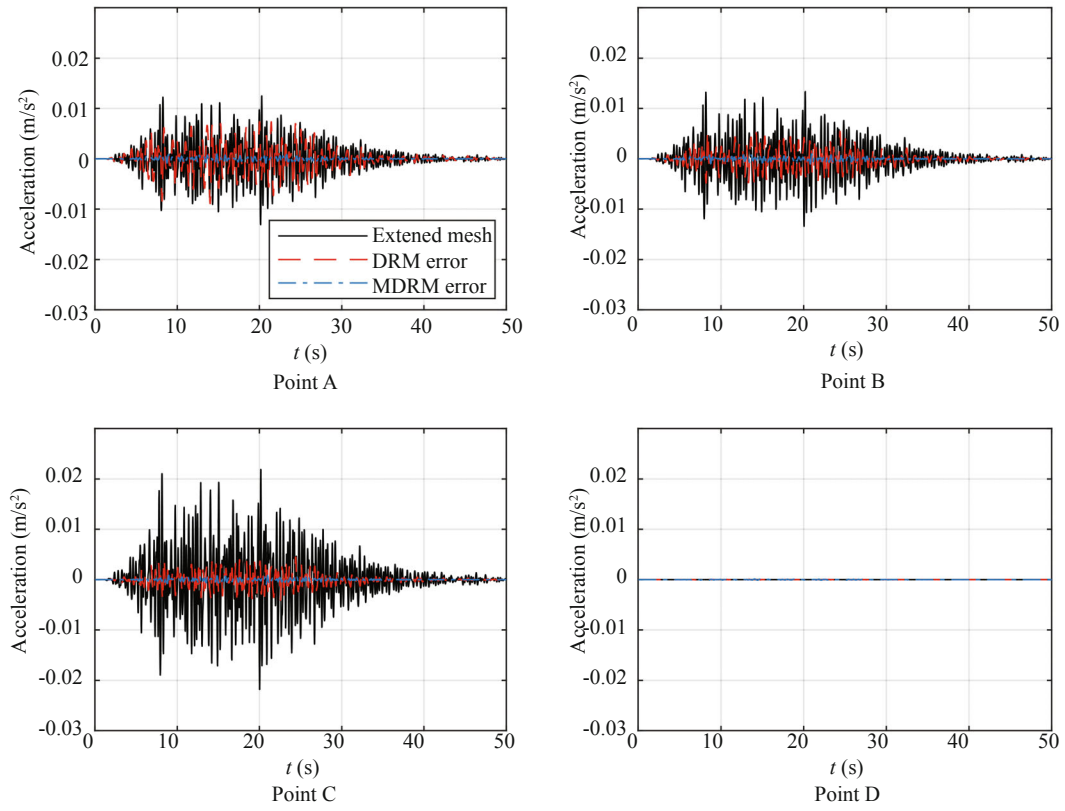

Fig. 14 Comparison of vertical acceleration time history in case 4

Table 3 PGA errors comparison of case 1 (%)

Directions	Methods	A	B	C	D
Horizontal	DRM	0.167	-0.359	-0.537	-0.076
	MDRM	0.029	0.035	0.048	0.033
Vertical	DRM	-1.727	4.460	0.980	
	MDRM	-0.057	-0.038	0.008	

Table 4 PGA errors comparison of case 2 (%)

Directions	Methods	A	B	C	D
Horizontal	DRM	0.447	-0.562	-1.238	-1.241
	MDRM	0.014	0.018	0.035	0.028
Vertical	DRM	-2.324	9.722	2.887	
	MDRM	-0.166	-0.075	-0.012	

Table 5 PGA errors comparison of case 3 (%)

Directions	Methods	A	B	C	D
Horizontal	DRM	-1.334	-1.606	-1.395	-1.100
	MDRM	-0.118	0.130	0.261	0.386
Vertical	DRM	-6.772	-9.037	-0.897	
	MDRM	2.136	-1.605	-1.671	

has a large number of zero crossing times, for example the seismic wave shown in Fig. 3, these residual waves will be accumulated on the upcoming peaks and increase the computation error. This is the reason that the error calculated by bedrock motion is greater than that by Ricker wave.

In conclusion, the MDRM has a relatively higher accuracy than the DRM. The DRM can produce an error of more than 30% in practice. Attention should be paid when applying the DRM, and the recommendation is to use the MDRM instead if possible.

4 Comparison with two conventional methods

In this section, the performance of MDRM is compared with two widely used artificial boundaries; that is, Liao's transmitting boundary (Liao *et al*., 1984) and the viscous boundary (Lysmer *et al*., 1969). As mentioned above, Liao's transmitting boundary is suitable for both internal and external source problems. Though the viscous boundary was originally designed for internal source problems, Liu *et al*. (Liu *et al*., 1998) proposed a method using a viscous-spring boundary with equivalent forces to simulate seismic wave input with any angle, which makes the viscous-spring available for external source problems. The implementation details of these two methods can be found in the references (Liao *et al*., 1984; Lysmer *et al*., 1969; Liu *et al*., 1998) and will not be repeated here.

As mentioned above, the MDRM has to be used with suitable absorbing boundary conditions and a viscous-spring boundary was used in the previous section. To clarify, Liao's transmitting boundary, viscous-spring boundary with Liu's method and the MDRM with viscous-spring boundary are compared in this section and are denoted as transmitting boundary, viscous-spring boundary and MDRM, respectively. Case 3 is recalculated by these three methods. Likewise, the results of the extended meshed model are regarded as the accurate results.

Table 7 shows the horizontal and vertical PGA error of each method. The results of the extended meshed model and the absolute error of the three methods at point A are shown in Figs. 15 and 16. Due to space constraints, the results at Point B, C and D, similar to Point A, are not plotted here.

The results in Fig. 15 and Table 7 demonstrate that all three methods have high accuracy in the horizontal direction, and it can be seen from Fig. 16 and Table 7 that the maximum error of the MDRM, the transmitting boundary and the viscous-spring boundary in the vertical

Table 6 PGA errors comparison of case 4 (%)

Directions	Methods	A	B	C	D
Horizontal	DRM	-1.490	-1.600	-1.703	-2.093
	MDRM	-0.060	0.003	0.054	0.108
Vertical	DRM	-22.766	-32.441	-12.821	
	MDRM	1.638	-0.661	-1.173	

Table 7 PGA errors comparison (%)

Directions	Methods	A	B	C	D
Horizontal	MDRM	-0.118	0.130	0.261	0.386
	Transmitting boundary	0.096	0.380	0.598	0.944
	Viscous-spring boundary	-0.655	-0.725	-0.423	0.136
Vertical	MDRM	2.136	-1.605	-1.671	
	Transmitting boundary	8.745	3.473	-1.526	
	Viscous-spring boundary	-7.557	-1.206	2.330	

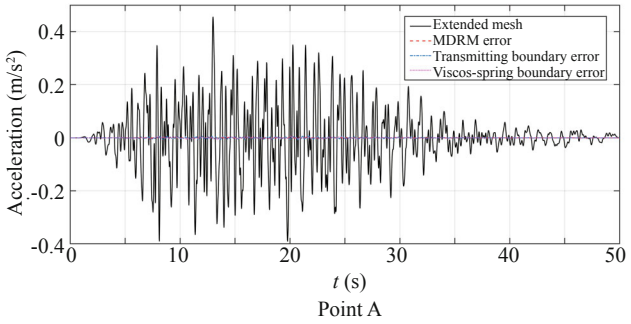

Fig. 15 Comparison of horizontal acceleration time history at point A

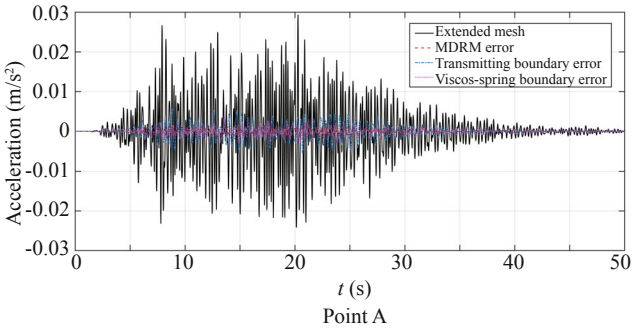

Fig. 16 Comparison of vertical acceleration time history at point A

direction is 2.136% 8.745% and 7.557%, respectively. These errors indicate that the MDRM has better accuracy than the transmitting boundary and the viscous-spring boundary.

The MDRM has advantages not only in computational accuracy, but also in other aspects. It is well known that the transmitting boundary has drift instability and oscillation instability and its robustness needs to be improved. The elimination measures for these problems have been discussed (Liao *et al*., 1992; Guan *et al*., 1996; Li *et al*., 1996; Zhou *et al*., 2001; Liao *et al*., 2002; Jing *et al*., 2002; Xie *et al*., 2017). When using this method, researchers have to be very careful to avoid the potential drift and oscillation effects. On the other hand, Liu's method with viscous-spring boundary has good accuracy and stability, but can only be used in incident seismic wave input problems. The MDRM, however, can deal with any type of wave propagation with high accuracy and its robustness is very good. All in all, the MDRM is more advanced than the two conventional methods.

5 Discussion of the location of MDRM boundary

Based on the results obtained above, the advantage of the MDRM in accuracy, efficiency and stability when simulating seismic wave propagation is clear. However, using the MDRM in practice needs more investigation. The DRM is a widely used method, yet the appropriateness of placing the DRM boundary layer close to the domain of interest has not been discussed, as well as the proper location of the MDRM boundary layer. When the DRM was first proposed (Bielak *et al*., 2003; Yoshimura *et al*., 2003), the DRM boundary layer was placed right at the edge of the topography. Jeremić *et al*. separated the whole soil domain into four domains for each pier of a bridge to save computation cost (Jeremić *et al*., 2009). When using DRM, researchers often truncate the computation domain as much as possible without verification. In this section, preliminary tests are conducted to determine whether the location of the MDRM boundary influences its computational accuracy.

First, the model in the previous section is truncated to study the influence of the MDRM boundary layer location, as shown in Fig. 17. In this truncated model, the MDRM boundary layer is located at the outer edge of the local topography. Since this model is the minimum model that was able to contain the local topography, it is named min-model here. Obviously, observation point A does not exist in the min-model.

The analysis of case 1 and case 3 is repeated with the min-model. The PGA errors of the min-model are shown in Table 8. A comparison of the time history for case 1 is shown in Fig. 18. The extended mesh results and the absolute error of the min-model for case 3 are shown in Fig. 19. The PGA errors of the min-model in both the horizontal and vertical directions are higher than those of the original model. It is clearly seen that the smaller model tends to have larger errors. The maximum PGA error of the min-model is 28.331% as shown in Table 8, which is not acceptable for most circumstances.

To further investigate the influence of the MDRM boundary layer location, the errors of models with different sizes were calculated for case 3. The model sizes and the corresponding errors are shown in Table 9. From the results in Table 9, it can be concluded that the error increases as the model size decreases. The

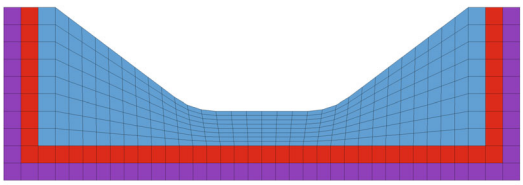

Fig. 17 Finite element mesh of min-model

Table 8 PGA errors of min-model (%)

	Directions	B	C	D
Case1	Horizontal	-6.766	-7.682	-1.920
	Vertical	-28.331	-13.107	
Case3	Horizontal	-2.738	-3.563	-2.403
	Vertical	-19.323	-3.170	

results also show that a model that is 300 m×180 m has good performance in both accuracy and efficiency when incorporated with the MDRM.

Since the observation points are located in different positions, it is necessary to define a rational parameter to assess the relationship between the computational accuracy and the size of the model. Therefore, two dimensionless parameters, φ_1 and φ_2, are defined by the following equations:

Table 9 PGA errors of different model size of case 3

Directions	Model size (m)	B	C	D
Horizontal	400×240	-0.130	-0.261	-0.386
	300×180	-0.231	0.124	0.589
	200×120	-0.726	-0.256	0.329
	100×60	0.746	0.414	1.672
	65×20 (min-model)	-2.738	-3.563	-2.403
Vertical	400×240	1.605	1.671	
	300×180	-0.673	0.116	
	200×120	6.913	3.396	
	100×60	-11.274	-8.715	
	65×20 (min-model)	-19.323	-3.170	

$$\varphi_1=\frac{d_b}{d_v} \tag{12}$$

$$\varphi_2=\frac{h_b}{h_v} \tag{13}$$

where d_b denotes the horizontal distance from the observation point to the MDRM boundary; d_y denotes the width of the idealized valley; h_b denotes the vertical distance from the observation point to the MDRM valley; and h_y denotes the depth of the idealized valley. φ_1 indicates the dimensionless relationship between the model size in the horizontal direction and the width of the topography; and φ_2 indicates the dimensionless relationship between the model size in the vertical direction and the depth of the topography. Since the locations of the four observations points are different, these observation points have different values of φ_1 and φ_2 even in the same model. The relationship between φ_1 (φ_2) and the absolute value of the PGA error are shown in Figs. 20 and 21.

From Figs. 20 and 21, it is seen that the relationship between φ_1 (φ_2) and PGA error is not linear, but in general, the PGA error decreases as φ_1 and φ_2 increase.

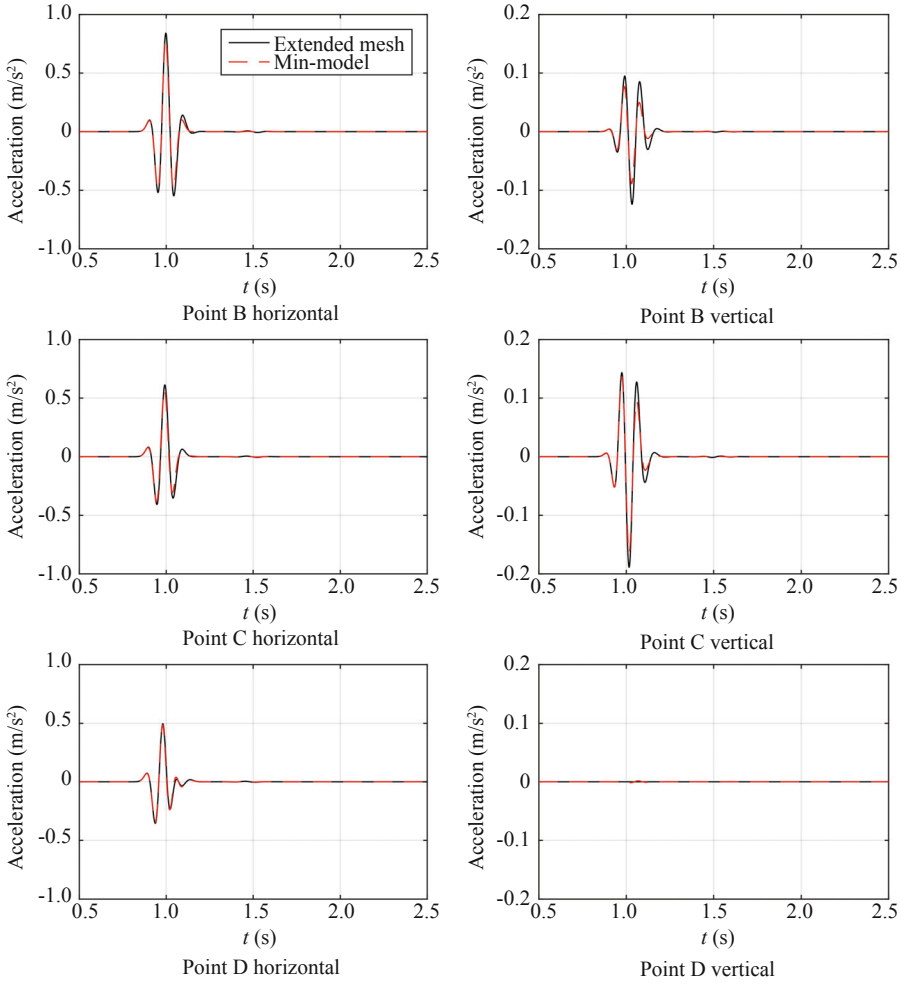

Fig. 18 Comparison of acceleration time history of case 1

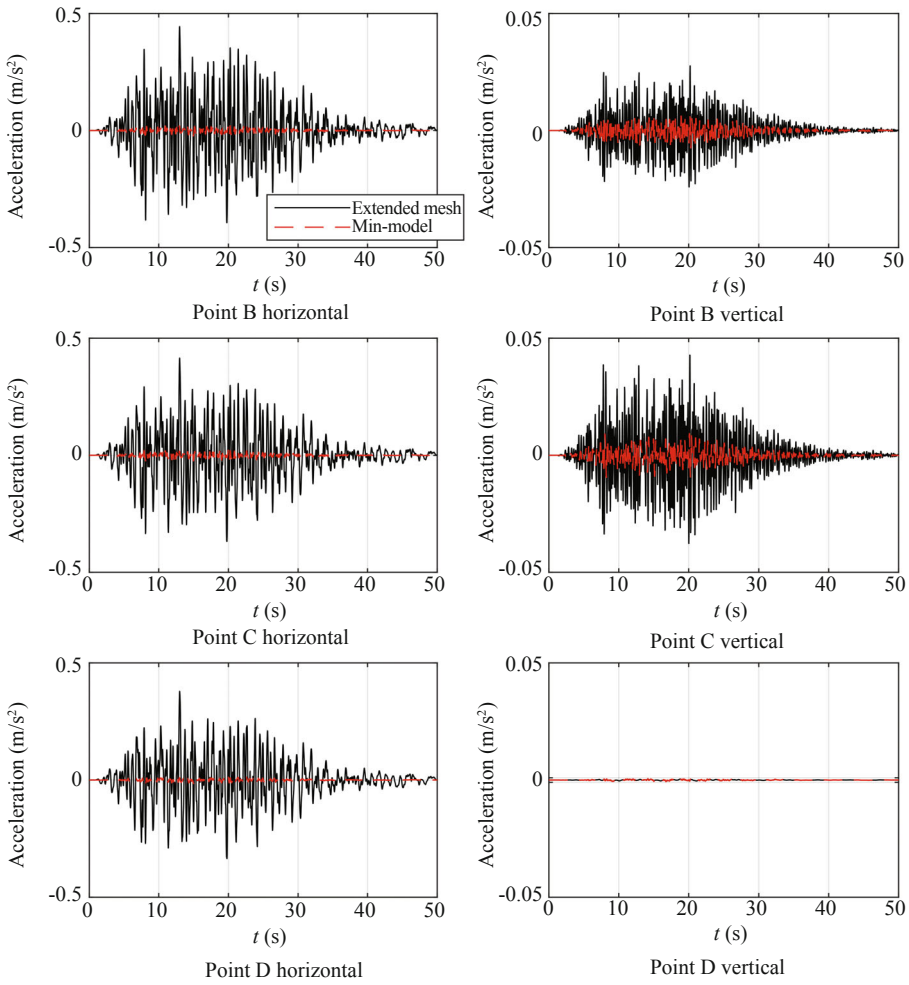

Fig. 19 Comparison of acceleration time history of case 3

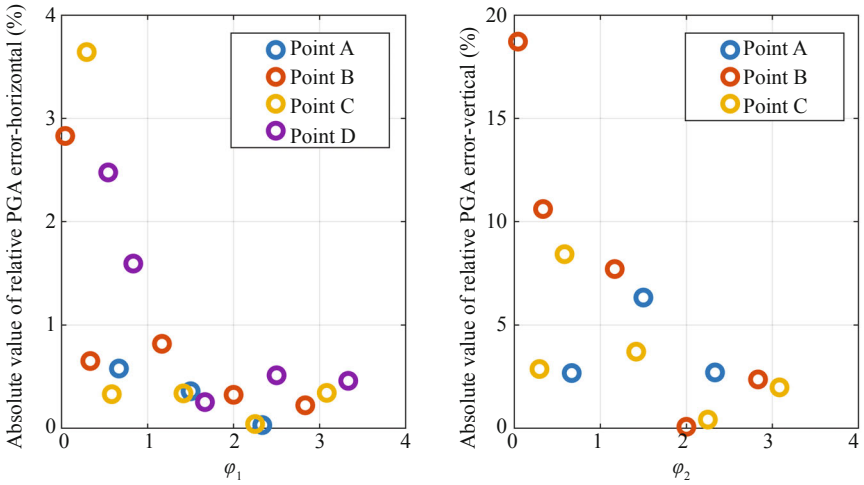

Fig. 20 Absolute value of horizontal and vertical PGA errors with different φ_1

When the damping ratio is 5%, the relative horizontal PGA error can be limited to 1% when $\varphi_1 > 1$ or $\varphi_2 > 5$ and the relative vertical PGA error can be limited to 5% when $\varphi_1 > 2$ or $\varphi_2 > 13$. In practice, the location of the MDRM boundary can be set as defined above to achieve the desired accuracy.

Other than φ_1 and φ_2, the damping ratio of the material may also have an influence on the computational accuracy. To investigate how the damping ratio influences the computational accuracy, the errors of models with different sizes and material damping were calculated. The model sizes, damping ratio and corresponding errors

are shown in Table 10. The relationship between φ_1 (φ_2) and the absolute value of the PGA errors are shown in Figs. 22 and 23.

From the results in Figs. 22 and 23, Table 9 and Table 10, it can be concluded that in general, the PGA errors increase as the damping ratio decreases, whereas the PGA error is much more sensitive to the change in φ_1 and φ_2 than the change of the damping ratio. In

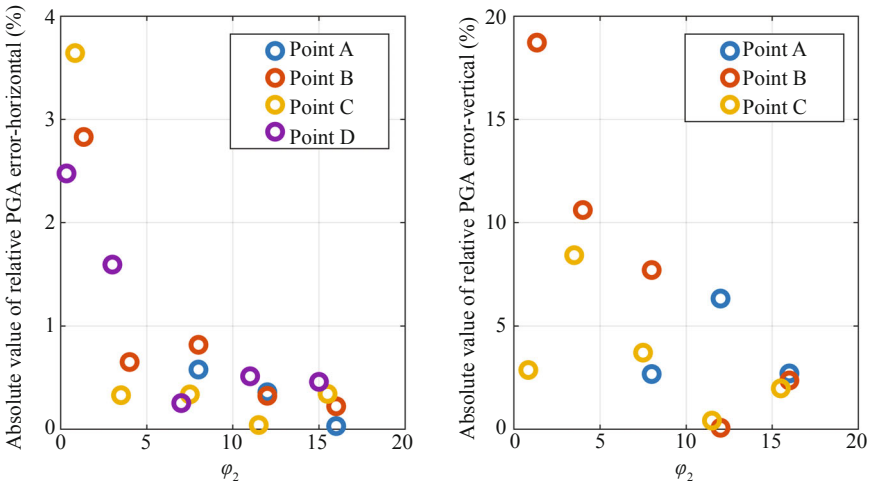

Fig. 21 Absolute value of horizontal and vertical PGA errors with different φ_2

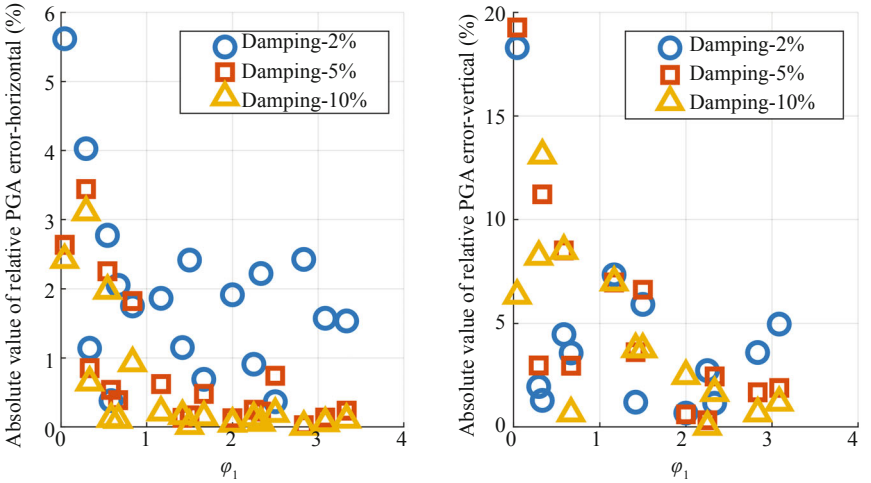

Fig. 22 Absolute value of horizontal and vertical PGA errors with different φ_1 and damping ratio

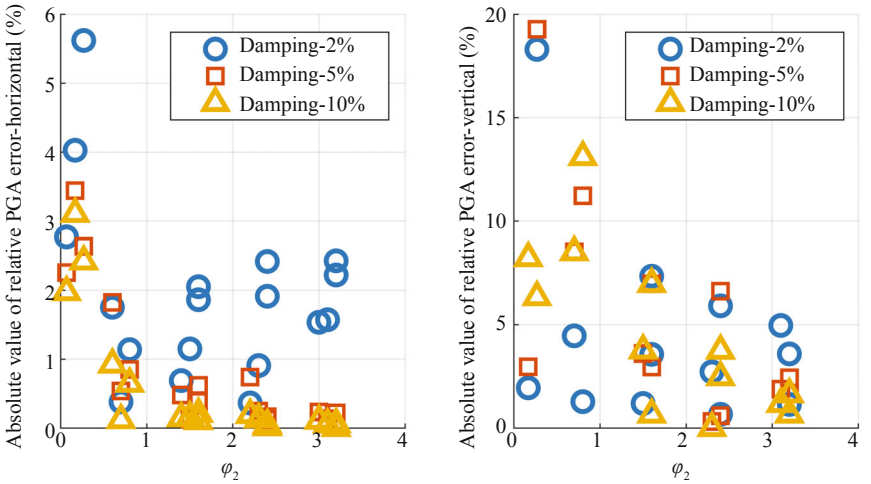

Fig. 23 Absolute value of horizontal and vertical PGA errors with different φ_2 and damping ratio

Table 10 PGA errors of model with different size and damping ratio

Directions	Model size (m)	2%			10%		
		B	C	D	B	C	D
Horizontal	400×240	-2.428	-1.573	-1.536	-0.003	-0.054	-0.108
	300×180	-1.914	-0.909	0.366	0.047	0.130	0.192
	200×120	-1.863	-1.150	0.691	-0.209	-0.158	-0.143
	100×60	-1.140	0.381	1.754	0.646	0.117	0.923
	65×20 (min-model)	-5.619	-4.027	-2.773	-2.420	-3.105	-1.974
Vertical	400×240	3.592	4.968		0.661	1.173	
	300×180	-0.671	2.724		2.466	0.009	
	200×120	7.347	1.196		6.976	3.762	
	100×60	-1.284	-4.466		-13.097	-8.507	
	65×20 (min-model)	-18.299	-1.952		-6.338	8.224	

practice, the damping ratio is not a crucial factor for PGA errors. Given that the damping ratio of most sites is equal to or greater than 2%, in engineering practice the relative horizontal PGA error can be limited to 3% when $\varphi_1 > 1$ or $\varphi_2 > 5$ and the relative vertical PGA error can be limited to 5% when $\varphi_1 > 2$ or $\varphi_2 > 13$.

The preliminary test results indicate that artificial boundaries should be used in an appropriate way. According to the results above, when performing site response analysis in a valley topography using the MDRM, the finite element model size can be determined through two dimensionless parameters, φ_1 and φ_2, to achieve the desired computational accuracy.

6 Conclusions

A MDRM for simulating seismic wave propagation was presented by introducing the damping terms to the DRM. The computational accuracy of the DRM and the MDRM were compared with a SV wave propagation model. Both the DRM and the MDRM show high accuracy in the response of the horizontal direction. In the vertical direction, the accuracy of the DRM decreases as the damping ratio increases and zero crossing times of input motion. The maximum acceleration error of the DRM in the vertical direction can be as high as 32.441% while that of the MDRM is only 2.136%. Overall, the MDRM shows much higher accuracy than the DRM.

Furthermore, the accuracy of the MDRM was compared with Liao's transmitting boundary and viscous-spring boundary with Liu's method. The results show that all three methods have the ability to simulate seismic wave propagation but the MDRM was superior in terms of accuracy, stability and the range of applications.

Finally, a preliminary test was performed to investigate the influence of the boundary location on computational accuracy. By analyzing models of different sizes, it can be seen that an error that potentially exceeds 25% could occur if the MDRM boundary layer is located too close to the local topography. Two dimensionless parameters, φ_1 and φ_2, are introduced. When $\varphi_1 > 2$ or $\varphi_2 > 13$, the PGA errors are limited to 5%. In practice, researchers and engineers can estimate the computational accuracy by φ_1 and φ_2.

Acknowledgement

The financial support provided by the China Scholarship Council for Dr. Luo Chao′s two-year visit in the University of California, Davis is greatly appreciated. This work presented was sponsored by the National Natural Science Foundation of China under grant Nos. 91315301, 51478279 and the State Key Laboratory Basic Theory Foundation of the Ministry of Science and Technology of China under the grant SLDRCE08-A-07. These supports are gratefully acknowledged.

References

Berenger and Jean-Pierre (1994), "A Perfectly Matched Layer for the Absorption of Electromagnetic Waves," *Journal of computational physics*, **114**(2): 185–200.

Bielak J, Loukakis K, Hisada Y and Yoshimura C (2003), "Domain Reduction Method for Three-dimensional Earthquake Modeling in Localized Regions, Part I: Theory," *Bulletin of the Seismological Society of America*, **93**(2): 817–824.

Corigliano M, Scandella L, Lai CG and Paolucci R (2011), "Seismic Analysis of Deep Tunnels in Near Fault Conditions: A Case Study in Southern Italy," *Bulletin of Earthquake Engineering*, **9**(4): 975–995.

Deeks AJ and Randolph MF (1994), "Axisymmetric Time-Domain Transmitting Boundaries," *Journal of Engineering Mechanics*, **120**(1): 25–42.

Farzanian M, Arbabi F and Pak R (2016), "PML Solution

of Longitudinal Wave Propagation in Heterogeneous Media," *Earthquake Engineering and Engineering Vibration*, **15**(2): 357–368.

Guan Huimin and Liao Zhenpeng (1996), "A Method for the Stability Analysis of Local Artificial Boundaries," *Chinese Journal of Theoretical and Applied Mechanics*, **28**(3): 121–125. (in Chinese)

Hilber HM , Hughes TJ and Taylor RL (1977), "Improved Numerical Dissipation for Time Integration Algorithms in Structural Dynamics," *Earthquake Engineering & Structural Dynamics*, **5**(3): 283–292.

Huang J, Zhao M, Xu C, Du X, Jin L and Zhao X (2018), "Seismic Stability of Jointed Rock Slopes under Obliquely Incident Earthquake Waves," *Earthquake Engineering and Engineering Vibration*, **17**(3): 527–539.

Idriss IM and Seed HB (1968), "Seismic Response of Horizontal Soil Lauers," *ASCE Journal of Soil Mechanics*, **94**(4): 1003–1031.

Isbiliroglu Y, Taborda R and Bielak J (2015), "Coupled Soil-Structure Interaction Effects of Building Clusters During Earthquakes," *Earthquake Spectra*, **31**(1): 463–500.

Jeremić B, Jie G, Preisig M and Tafazzoli N (2009), "Time Domain Simulation of Soil-Foundation-Structure Interaction in Non-Uniform Soils," *Earthquake Engineering & Structural Dynamics*, **38**(5): 699–718.

Jeremić B, Tafazzoli N, Ancheta T, Orbović N and Blahoianu A (2013), "Seismic Behavior of NPP Structures Subjected to Realistic 3D, Inclined Seismic Motions, in Variable Layered Soil/Rock, on Surface or Embedded Foundations," *Nuclear Engineering and Design*, **265**: 85–94.

Jeremić B, Yang Z, Cheng Z, Jie G and Sett K (2015), *Lecture Notes on Computational Geomechanics: Inelastic Finite Elements for Pressure Sensitive Materials*, Department of Civil & Environmental Engineering, University of California at Davis, California.

Jing Liping, Liao Zhenpeng and Zou Jingxiang (2002), "A High-Frequency Instability Mechanism in Numerical Realization of Multi-Transmitting Formula," *Earthquake Engineering and Engineering Vibration*, **22**(1): 7–13. (in Chinese).

Joyner WB and Chen AT (1975), "Calculation of Nonlinear Ground Response in Earthquakes," *Bulletin of the Seismological Society of America*, **65**(5): 1315–1336.

Kausel E (1988), "Local Transmitting Boundaries," *Journal of Engineering Mechanics*, **114**(6): 1011-1027.

Kellezi L (2000), "Local Transmitting Boundaries for Transient Elastic Analysis," *Soil Dynamics and Earthquake Engineering*, **19**(7): 533–547.

Kontoe S, Zdravkovic L and Potts DM (2008), "The Domain Reduction Method for Dynamic Coupled Consolidation Problems in Geotechnical Engineering," *International Journal for Numerical and Analytical Methods in Geomechanics*, **32**(6): 659–680.

Kontoe S, Zdravkovic L and Potts DM (2009), "An Assessment of the Domain Reduction Method as an Advanced Boundary Condition and Some Pitfalls in the Use of Conventional Absorbing Boundaries," *International Journal for Numerical and Analytical Methods in Geomechanics*, **33**(3): 309–330.

Kontoe S, Zdravkovic L, Menkiti CO and Potts DM (2012), "Seismic Response and Interaction of Complex Soil Retaining Systems," *Computers and Geotechnics*, **39**: 17–26.

Li Xiaojun and Liao Zhenpeng (1996), "Calculate the Drift Instability of Local Transmitting Boundary in Time Domain," *Chinese Journal of Theoretical and Applied Mechanics*, **28**(5): 627–632. (in Chinese)

Liang F, Chen H and Huang M (2017), "Accuracy of Three-Dimensional Seismic Ground Response Analysis in Time Domain Using Nonlinear Numerical Simulations," *Earthquake Engineering and Engineering Vibration*, **16**(3): 487–498.

Liao ZP and Wong HL (1984), "A Transmitting Boundary for the Numerical Simulation of Elastic Wave Propagation," *Soil Dynamics and Earthquake Engineering*, **3**(4): 174–183.

Liao ZP and Liu JB (1992), "Numerical Instabilities of a Local Transmitting Boundary," *Earthquake Engineering & Structural Dynamics*, **21**(1): 65–77.

Liao ZP, Wong HL, Yang BP and Yuan YF (1984), "A Transmitting Boundary for Transient Wave Analysis," *Scientia Sinica*, **27**(10): 1063–1076.

Liao ZP, Zhou ZH and Zhang YH (2002), "Stable Implementation of Transmitting Boundary in Numerical Simulation of Wave Motion," *Chinese Journal of Geophysics*, **45**(4): 554–568.

Liu JB and Lv YD (1998), "A Direct Method for Analysis of Dynamic Soil-Structure Interaction Based on Interface Idea." *Dynamic Soil-Structure Interaction-Current Research in China and Switzerland*, Elsevier.

Lindman EL (1975), "Free-Space Boundary-Conditions for Time-Dependent Wave-Equation," *Journal of Computational Pysics*, **18**(1): 66–78.

Liu JB, Du YX, Du XL, Wang ZY and Wu J (2006), "3D Viscous-spring Artificial Boundary in Time Domain," *Earthquake Engineering and Engineering Vibration*, **5**(1): 93–102.

Lysmer J (1978), *Analytical Procedures in Soil Dynamics*, University of California at Berkeley, Earthquake Engineering Research Center, Richmond, CA.

Lysmer J and Kuhlemeyer RL (1969), "Finite Dynamic Model for Infinite Media," *Journal of the Engineering Mechanics Division*, **95**(4): 859–878.

Mavroeidis GP and Papageorgiou AS (2003), "A Mathematical Representation of Near-Fault Ground Motions," *Bulletin of the Seismological Society of America*, **93**(3): 1099–1131.

Newmark NM (1959), "A Method of Computation

for Structural Dynamics," *Journal of the Engineering Mechanics Division*, **85**(3): 67–94.

Poursartip B, Fathi A and Kallivokas LF (2017), "Seismic Wave Amplification by Topographic Features: A Parametric Study," *Soil Dynamics and Earthquake Engineering*, **92**: 503–527.

Smerzini C, Paolucci R and Stupazzini M (2011), "Comparison of 3D, 2D and 1D Numerical Approaches to Predict Long Period Earthquake Ground Motion in the Gubbio Plain, Central Italy," *Bulletin of Earthquake Engineering*, **9**(6): 2007–2029.

Solberg JM, Hossain Q and Mseis G (2016), "Nonlinear Time-domain Soil–Structure Interaction Analysis of Embedded Reactor Structures Subjected to Earthquake Loads," *Nuclear Engineering and Design*, **304**: 100–124.

Xie ZN and Zhang XB (2017), "Analysis of High-Frequency Local Coupling Instability Induced by Multi-Transmitting Formula–P-SV Wave Simulation in a 2D Waveguide." *Earthquake Engineering and Engineering Vibration*, **16**(1): 1–10.

Yasui Y, Takano S, Takeda T, Miyamoto A, Kurimoto O and Ishikawa R (1988), "Finite Element Method for Obliquely Incident Seismic Wave Problems," *Proceedings of the Ninth World Conference on Earthquake Engineering*, Japan.

Yoshimura C, Bielak J, Hisada Y and Fernandez A (2003), "Domain Reduction Method for Three-Dimensional Earthquake Modeling in Localized Regions, Part II: Verification and Applications," *Bulletin of the Seismological Society of America*, **93**(2): 825–840.

Zhou Zhenghua and Liao Zhenpeng (2001), "A Measure for Eliminating Drift Instability of the Multi-Transmitting Formula," *Chinese Journal of Theoretical and Applied Mechanics*, **33**(4): 550–554. (in Chinese)